



# Comparison of thermoresponsive Diels-Alder linkers for the release of payloads from magnetic nanoparticles via hysteretic heating

Julien H. Arrizabalaga<sup>a</sup>, Jonathan S. Casey<sup>a</sup>, Jeffrey C. Becca<sup>b</sup>, Lasse Jensen<sup>b</sup>, Daniel J. Hayes<sup>a,c,d,\*</sup>

<sup>a</sup> The Department of Biomedical Engineering, The Pennsylvania State University, University Park, PA, 16802, United States

<sup>b</sup> The Department of Chemistry, The Pennsylvania State University, University Park, PA, 16802, United States

<sup>c</sup> Materials Research Institute, Millennium Science Complex, The Pennsylvania State University, University Park, PA, 16802, United States

<sup>d</sup> The Huck Institute of the Life Sciences, Millennium Science Complex, The Pennsylvania State University, University Park, PA, 16802, United States

## ARTICLE INFO

### Keywords:

Diels-alder  
Click chemistry  
Alternating magnetic field  
Controlled release  
Iron oxide  
Magnetic nanoparticles

## ABSTRACT

Investigation into the use of thermally reversible Diels-Alder chemistry coupled with magnetic iron oxide nanoparticles has grown over the last decade. This technology has been used for a variety of applications such as thermoresponsive materials, catalytic chemistry, and drug delivery systems. In this study, we evaluate two distinct thermally labile Diels-Alder linkers for the release of payloads from the surface of magnetic iron oxide nanoparticles. Density functional theory (DFT) computational predictions of the Gibbs free energy and enthalpy reaction barriers were performed and revealed a dramatic difference in reverse energy barriers between the two linkers. These thiophene-based cycloadducts were then synthesized, conjugated to the surface of iron oxide nanoparticles, and characterized by NMR and ESI-MS. The results of the modeling were confirmed when the functionalized nanoparticles were subjected to immersion heating and the payload release rates observed were in agreement with the DFT calculations. Similarly, AMF-RF hysteretic heating of the functionalized nanoparticles revealed payload release rates that correlated with the DFT calculations and the data from the heat immersion studies. Together, these results indicate that these distinct thermally labile Diels-Alder linkers can be used to fine-tune the kinetics of payload release from nanoparticles.

## 1. Introduction

Thermally reversible Diels-Alder chemistry used in combination with iron oxide nanoparticles have been investigated over the last decade for a variety of applications including thermally responsive self-healing nanocomposites [1–3], drug delivery systems [4–12], catalytic chemistry [13,14], and macromolecular materials [15]. Magnetic nanoparticles can be used to modulate Diels-Alder and retro Diels-Alder reactions through localized heating via Brownian motion and Néel relaxation mechanisms when stimulated by an externally applied alternating magnetic field radiofrequency (AMF-RF) [16]. The heat generated by the magnetic nanoparticles promotes the Diels-Alder or retro Diels-Alder reaction on their surface. In a recently reported study, iron oxide nanoparticles and Diels-Alder cycloadducts were conjugated to form a thermally responsive material [17]. Using iron oxide nanoparticles with anchored phosphonic acid groups, a network of furan-maleimide Diels-Alder cycloadducts was connected to discrete iron oxide nanoparticles.

The resulting material underwent retro Diels-Alder reactions and decompositions at 120 °C as demonstrated by differential scanning calorimetry. Having reversible cross-linked networks, with cross-linked iron oxide magnetic nanoparticles would be a significant benefit in self-healing and drug releasing technology.

Given the ease and specificity in which they occur, Diels-Alder reactions have been labeled “click chemistry” reactions [18]. Iron oxide nanoparticles and Diels-Alder linkers have been reported in the literature to form supramolecular complexes [15]. The Diels-Alder modified nanoparticles were attached to larger silica dioxide nanoparticles at multiple attachment points. For disassembly of the modified iron oxide nanospheres, the particles were heated up to 130 °C in DMSO for 24 h. The attachment efficiency and release rates of the spheres were dependent on the Diels-Alder cycloadducts linking the discrete nanoparticles together. Decreasing the energy barriers of the retro Diels-Alder would allow for either heat immersion or AMF-RF heating to dislocate the modified iron oxide nanoparticle spheres. Lowering the energy barrier of

\* Corresponding author. Materials Research Institute, Millennium Science Complex, The Pennsylvania State University, University Park, PA, 16802, United States.  
E-mail address: [djh195@psu.edu](mailto:djh195@psu.edu) (D.J. Hayes).

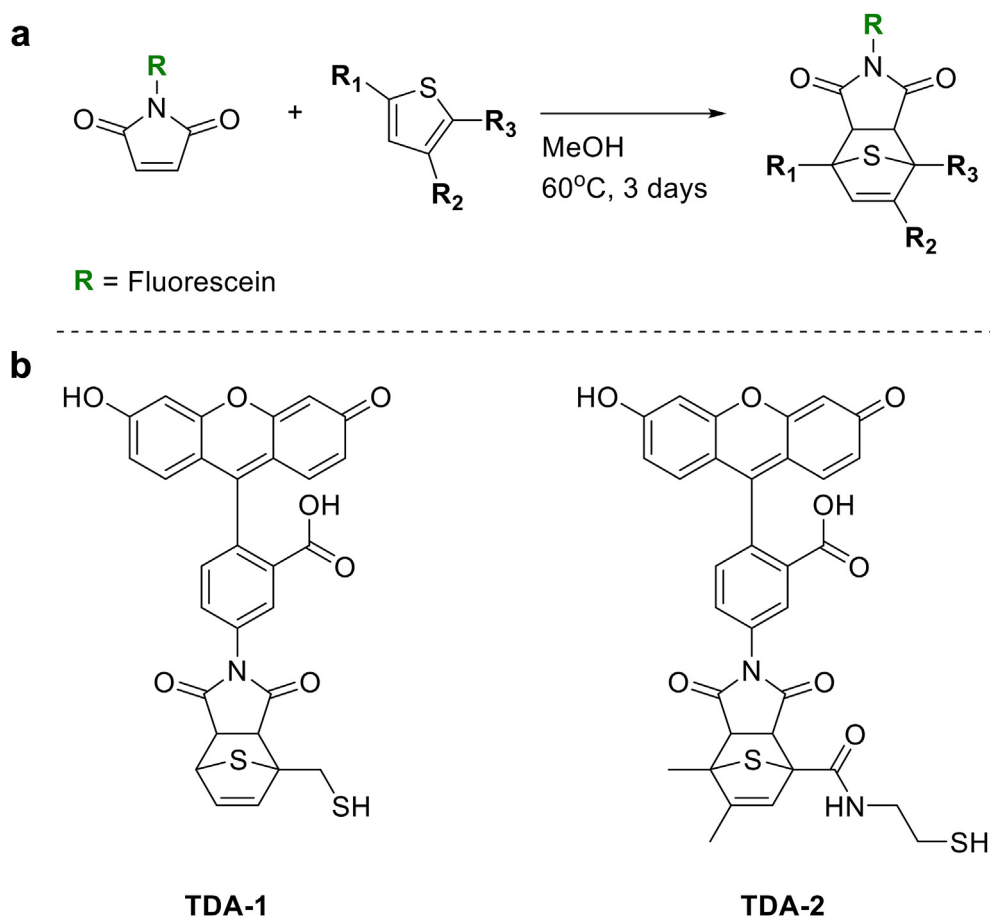


**Fig. 1.** a) General cycloaddition reaction between a thiophene-based diene and fluorescein maleimide. b) Structures of both cycloadducts named TDA-1 and TDA-2 used in this study.

release for these spheres could be accomplished by using different Diels-Alder cycloadducts. Benefits of this technology have been reported in the literature and have possible applications in optics (i.e. imaging), catalysis, or medicine [19–24].

In another study comparing Diels-Alder cycloadducts, substituting the central atom (N, O, or S) of the diene had dramatic consequences in terms of reverse energy barriers [25]. Similarly, in studies using similar cycloadducts on the surface of silver nanoparticles, the payload release rate after light activation and photothermal heating was correlated to the diene that was used to initially form the cycloadduct [26]. The experimental results showed that the pyrrole based Diels-Alder cycloadduct had the largest percentage of total release followed by the furan and lastly the thiophene-based cycloadduct, in correlation with the predicted energy barriers by density functional theory (DFT) calculations. Additionally, two different follow up studies were performed demonstrating controlled payload release using light activation *in vitro* and *in vivo* with silver nanoparticles and a furan-based Diels-Alder linker [27,28].

Studies demonstrating retro Diels-Alder mediated payload release using magnetic nanoparticles have also been reported [5,29]. In one study [5], the energy barriers of thiophene-based Diels-Alder linkers were modeled using DFT. The payload release rates from the surface of magnetic nanoparticles were predicted from these calculations and aligned with the specific loss power (SLP) values from the different magnetic nanoparticles used. A similar study demonstrated that a furfuryl modified iron oxide nanoparticle could release a rhodamine payload through a retro Diels-Alder reaction when heated above 60 °C [29].

In this study, we further develop the previously investigated [5,26] maleimide-based Diels-Alder cycloadducts but with two singular

thiophene-based dienes: 2-Thiophenemethanethiol (T-1) which was obtained commercially and 4,5-Dimethyl-N-(2-sulfanylethyl)-2-thiophene-carboxamide (T-2) which was synthesized (Fig. 1). To the best of our knowledge, the thiophene T-2 that was produced for this study has never been reported in the literature before. The retro Diels-Alder reactions with TDA-1 and TDA-2 were examined and compared on the surface of Fe<sub>3</sub>O<sub>4</sub> nanoparticles. Using density functional theory calculations, the forward and reverse energy barriers for these cycloadducts were predicted. TDA-1 had a high reverse energy barrier, while TDA-2 possessed a low one. Heat immersion and AMF-RF hysteretic heating experiments were then performed on the modified nanoparticles, with payload release rates correlating with the predicted DFT calculated energy barriers. Additionally, Zeta potentials were determined for each type of modified iron oxide nanoparticles, demonstrating characteristic surface charge for the two different Diels-Alder cycloadducts.

## 2. Materials and methods

### 2.1. Reagents

Iron (II) chloride tetrahydrate (98%), iron (III) chloride hexahydrate (≥98%), hydrochloric acid (HCl, ACS Reagent, 37%), (3-aminopropyl) triethoxysilane (APTES, 99%), dichloromethane (>99.8%), methanol (anhydrous, 99.8%), dimethyl sulfoxide (anhydrous DMSO, ≥99.9%), sodium carbonate (≥99.5%), 4,5-dimethylthiophene-2-carboxaldehyde (97%), cysteamine(95%), N,N-dimethylformamide (anhydrous, 99.8%), chloroform (≥99.5%), ethanol (≥99.5%), potassium permanganate (ACS Reagent, ≥99.0%), N-hydroxysuccinimide (NHS, 98%), N,N'-dicyclohexylcarbodiimide (99.0%), acetic acid (ACS Reagent, ≥99.7%), nitric

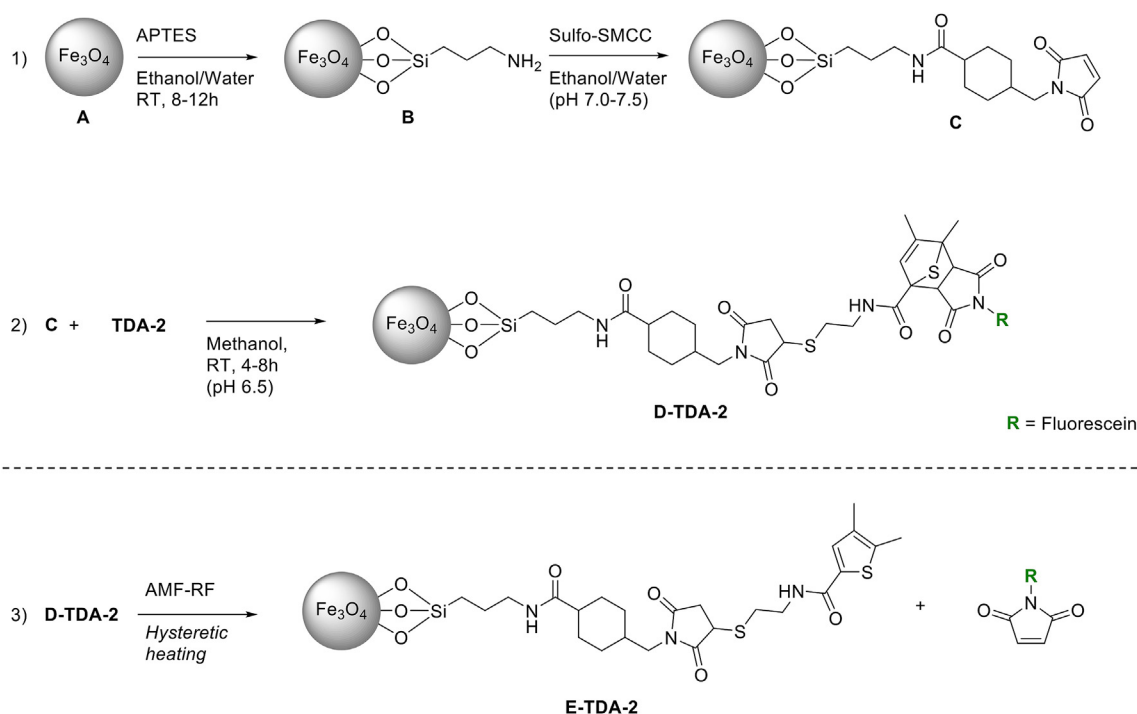


**Fig. 2.** 1) and 2): multistep functionalization of  $\text{Fe}_3\text{O}_4$  nanoparticles. Successive silanization step with APTES, conjugation of Sulfo-SMCC, and conjugation of the Diels-Alder linker TDA-2. A similar approach is used for the conjugation of TDA-1. 3): retro Diels-Alder cleavage reaction triggered by the AMF-RF hysteric heating and release of the fluorescein maleimide originally used for the preparation of TDA-2.

acid (ACS Reagent, 70%), ammonium hydroxide solution ( $\text{NH}_4\text{OH}$ , ACS reagent, 28.0–30.0%  $\text{NH}_3$  basis), tris(2-carboxyethyl)phosphine hydrochloride solution (TCEP, 0.5 M, pH 7.0 aqueous solution), and methanol-d4 ( $\geq 99.8$  atom % D) were purchased from Millipore Sigma (St Louis, MO). Sodium sulfite (ACS Reagent,  $\geq 98\%$ ) and sodium hydroxide ( $\geq 98\%$ ) were acquired from Honeywell Fluka (Morris Plains, NJ). Fluorescein-5-maleimide was obtained from Thermo Fisher Scientific (Waltham, MA), Sulfo-SMCC (Sulfosuccinimidyl-4-(N-maleimidomethyl) Cyclohexane-1-carboxylate) from Pierce Biotechnology (Rockford, IL), potassium phosphate monobasic (1.5 M) from Rigaku Reagents (Bainbridge Island, WA), *tert*-Butyl alcohol (99%) from Alfa Aesar (Tewksbury, MA), Dulbecco's Phosphate Buffered Saline (PBS) from Cytiva (Pittsburgh, PA), and 2-thiophenemethanethiol ( $>95\%$ ) from TCI America (Portland, OR). All reagents and solvents were used as received.

## 2.2. Computational methods

All DFT calculations were performed using the NWChem 6.8 software package [30]. All geometry optimizations and frequency calculations were performed using the B3LYP functional and a 6–311g\* basis set [31–34]. The numerical grid settings were set to extra fine and all optimizations were performed using tight convergence criteria for the gradient, gradient maximum, root mean square, and Cartesian step maximum. A reduced atom model was used for the maleimide to reduce computational effort and ensure no negative vibrational modes were found for the products and reactants, and just a single negative vibrational mode for transition states. Transition state searches were performed by using optimized structures of the reactants initially constrained to 2.4 Å apart measured at bond forming carbon atoms. The thermodynamic data was obtained during the normal mode analysis simulations at 25, 40, 60, and 80 °C. All simulations were performed excluding any solvent effects.

## 2.3. Synthesis of Diels-Alder linkers

Two different dienes were used in this study: 2-

Thiophenemethanethiol (T-1) which was obtained commercially and 4,5-Dimethyl-N-(2-sulfanylethyl)-2-thiophenecarboxamide (T-2) which was synthesized as described in the Supporting Material Fig. S1 [35,36]. The general cycloaddition reaction between a thiophene-based diene and fluorescein maleimide is illustrated in Fig. 1. TDA-1 was synthesized following a previously reported protocol with some minor modifications [5]. Briefly, 0.36  $\mu\text{L}$  of T-1 was combined with 5 mL of methanol in a glass vial. The pH of the solution was adjusted between 3.5 and 4 by addition of 1 M HCl. Fluorescein maleimide (2 mg) was then added to the glass vial prior to closing it, wrapping it in aluminum foil and heating it at 60 °C for 3 days. For the synthesis of TDA-2, 1.4 mg of T-2, 5  $\mu\text{L}$  of TCEP, and 5 mL of methanol were mixed in a glass vial. The pH was lowered between 3.5 and 4 by addition of 1 M HCl. Fluorescein maleimide (2 mg) was then added to the mixture. The glass vial was sealed, protected from light using aluminum foil, and heated at 60 °C in an oil bath for 3 days. The structures of TDA-1 and TDA-2 are reported in Fig. 1. Both cycloadducts were purified by column chromatography and characterized by NMR spectroscopy and electrospray ionization mass spectrometry (ESI-MS) as reported in the Supporting Material.

## 2.4. Synthesis of nanoparticles

$\text{Fe}_3\text{O}_4$  nanoparticles were synthesized by coprecipitation of  $\text{Fe}^{2+}$  and  $\text{Fe}^{3+}$  ions in presence of  $\text{NH}_4\text{OH}$  as previously reported [4,5,37]. Briefly, 2 mL of  $\text{FeCl}_2 \cdot 4\text{H}_2\text{O}$  (0.93 g) dissolved in 1 M HCl and 4 mL of  $\text{FeCl}_3 \cdot 6\text{H}_2\text{O}$  (2.16 g) dissolved in 1 M HCl were combined with 54 mL of deionized water in a round-bottom flask heated at 95 °C.  $\text{NH}_4\text{OH}$  (12.5 mL of 28%  $\text{NH}_3$  in  $\text{H}_2\text{O}$  solution) was slowly added and the mixture vigorously stirred for an hour. The solution was cooled down, and 1 M nitric acid was added to adjust the pH between 4 and 7. The mixture was then allowed to incubate at room temperature for 24 h. The nanoparticles were separated from the supernatant by centrifugation (30 min, 1300×g), and thoroughly washed three times with deionized water before getting dried. The X-ray diffraction patterns of the  $\text{Fe}_3\text{O}_4$  nanoparticles were obtained using a Malvern Panalytical Empyrean (3rd gen.) equipped with a Co source.  $\text{Fe}_3\text{O}_4$  nanoparticles were also characterized

**a**

		Reaction Barriers for $\Delta H_{rxn}$ (kcal/mol)				Reaction Barriers for $\Delta G$ (kcal/mol)			
Diels-Alder product	T (°C) Reaction	25	40	60	80	25	40	60	80
TDA-1 Exo	Forward	29.47	29.48	29.50	29.52	43.82	44.54	45.50	46.46
	Reverse	27.84	27.85	27.88	27.89	26.39	26.32	26.22	26.12
TDA-1 Endo	Forward	29.38	29.39	29.41	29.43	43.96	44.70	45.68	46.65
	Reverse	27.35	27.37	27.39	27.40	26.33	26.28	26.21	26.14
TDA-2 Exo	Forward	25.12	25.12	25.11	25.11	39.61	40.34	41.31	42.29
	Reverse	15.72	15.74	15.76	15.78	14.54	14.48	14.40	14.32
TDA-2 Endo	Forward	28.30	28.30	28.30	28.31	42.76	43.48	44.45	45.42
	Reverse	13.87	13.89	13.91	13.93	13.20	13.16	13.12	13.07

**b**

TDA-1 Exo      TDA-1 Endo      TDA-2 Exo      TDA-2 Endo

**Fig. 3.** a) Gibbs free energy and enthalpy reaction barriers generated from B3LYP/6-311G\* theory. b) Structures of endo and exo products for both TDA-1 and TDA-2 used for B3LYP/6-311G\* computation. Black atoms: Carbon; White: Hydrogen; Red: Oxygen; Blue: Nitrogen; Yellow: Sulfur. Images rendered using the software PyMOL. Transition states for these molecules are reported in the [Supporting Material Figure S2](#). (For interpretation of the references to colour in this figure legend, the reader is referred to the Web version of this article.)

using an FEI Tecnai G20 20 XTWIN transmission electron microscope. The magnetization of the nanoparticles was measured at 305 K using a Quantum Design MPMS system.

## 2.5. Functionalization of nanoparticles

The general functionalization protocol from bare Fe<sub>3</sub>O<sub>4</sub> nanoparticles to nanoparticles functionalized with either TDA-1 or TDA-2 is shown in [Fig. 2](#).

### 2.5.1. Silanization

The iron oxide nanoparticles were first functionalized by silanization following a previously established procedure [38]. Briefly, 5 mg of Fe<sub>3</sub>O<sub>4</sub> nanoparticles were dispersed by sonication in ethanol (10 mL) and water (66.5  $\mu$ L). APTES (2.69  $\mu$ L) was added to the mixture and the pH adjusted between 6 and 7 using 1 M HCl. The sealed polypropylene tube containing the solution was then placed on a rocker and mechanically agitated for 7 h at room temperature. The nanoparticles were separated from the

supernatant after centrifugation (10 min, 1200 $\times$ g), redispersed by sonication in anhydrous ethanol, and these washing steps repeated three times. After the final wash, the nanoparticles were dried under vacuum at room temperature for 8–12 h.

### 2.5.2. Conjugation of Sulfo-SMCC

Fe<sub>3</sub>O<sub>4</sub> nanoparticles modified with APTES were dispersed by sonication in ethanol (2.5 mL) and PBS (2.5 mL). The pH of the solution was adjusted between 7.2 and 7.5 before adding Sulfo-SMCC (5 mg), sealing the polypropylene tube containing the solution, and mechanically agitating it for 7 h on a rocker at room temperature. The nanoparticles were then centrifuged (10 min, 1200 $\times$ g), and washed with deionized water three times.

### 2.5.3. Conjugation of Diels-Alder linkers

Fe<sub>3</sub>O<sub>4</sub> nanoparticles previously modified with Sulfo-SMCC were pelleted down by centrifugation (10 min, 1200 $\times$ g) and the supernatant removed. The nanoparticles were redispersed by sonication in the Diels-



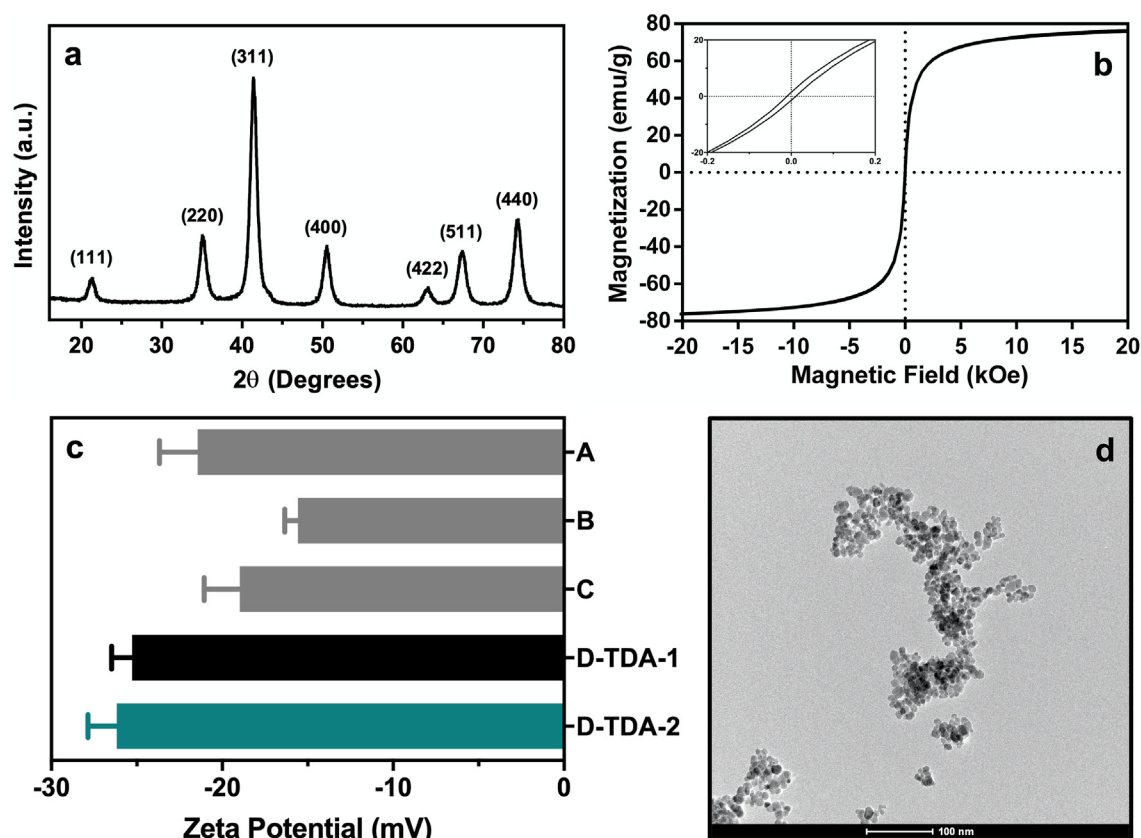


**Fig. 4.** Characterization of  $\text{Fe}_3\text{O}_4$  nanoparticles. a) X-ray diffraction patterns with representative index on typical peaks. b) Magnetic hysteresis curves with a zoom in the area of small magnetic fields in the inset panel. c) Zeta potential of nanoparticles during the different steps of the modification process. A, B, C, D-TDA-1, and D-TDA-2 refer to the nanoparticle functionalization steps as labeled in Fig. 2 d) TEM image of bare  $\text{Fe}_3\text{O}_4$  nanoparticles. Additional images are available in the Supporting Material Figure S3.

Alder mixture (5 mL of either TDA-1 or TDA-2) prepared in advance. The pH of the solution was adjusted between 6.5 and 6.6 using 1 M NaOH. The mixture was then put in a refrigerator at 4 °C and mechanically agitated for 12 h. The nanoparticles were then centrifuged (10 min, 1200×g) and washed seven times with chilled methanol at 4 °C before being redispersed in anhydrous DMSO before usage.

#### 2.5.4. Characterization of functionalized nanoparticles

Zeta potential measurements of the nanoparticles were carried out with a Malvern Zetasizer Nano ZS to monitor the change in surface charge at each conjugation step. Secondary Ion Mass Spectrometry (SIMS) analysis were performed as previously described to verify the successful functionalization of the  $\text{Fe}_3\text{O}_4$  nanoparticles [5,36,39]. Briefly, each sample was dried into a powder form, applied to a stage, and analyzed in positive ion mode at 70 keV using an Ionoptika J105 3D Chemical Imager.

#### 2.6. Immersion heating

$\text{Fe}_3\text{O}_4$  nanoparticles functionalized with either TDA-1 or TDA-2 were redispersed in anhydrous DMSO at a concentration of 50 ppm. Microcentrifuge tubes with 1 mL of nanoparticles in DMSO were prepared and heated at either 25 °C, 40 °C, 60 °C, or 80 °C for 1 h, 2 h, 4 h, or 6 h. Water baths were used for temperatures of 25 °C, 40 °C, and 60 °C but an oil bath was used for the 80 °C temperature to mitigate water evaporation. After immersion heating, samples were centrifuged (10 min, 1200×g), and three 100  $\mu\text{L}$  aliquots of the supernatant were pipetted per sample into a 96-well plate with 100  $\mu\text{L}$  of PBS added to each well. To evaluate the amount of fluorescein maleimide released by the retro Diels-Alder reaction (Fig. 2), the fluorescence intensity was measured in each

well at 494/518 nm (Excitation/Emission) using a Molecular Devices Spectramax M5 Microplate/Cuvette Reader.

#### 2.7. AMF-RF hysteretic heating

$\text{Fe}_3\text{O}_4$  nanoparticles functionalized with either TDA-1 or TDA-2 were redispersed in anhydrous DMSO at a concentration of 50 ppm. Microcentrifuge tubes with 1 mL of nanoparticles in DMSO were prepared and underwent AMF-RF hysteretic heating using a nanoTherics magneTherm. The radiofrequency was 624.7 kHz, the DC power supply current was 7.5 A, and the DC power supply voltage was 31 V. The AMF-RF coil used had a 50 mm diameter and 17 turns. The Alternating Magnetic Field Strength and the Specific Loss Power were determined as previously described [5, 40,41] and detailed protocols with equations are reported in the Supporting Material. The system was quasi-adiabatic, the heating device was connected to a recirculating water cooler which maintained the coil temperature at 15 °C during the operation of the equipment. The sample was encased in a Styrofoam receptacle before being inserted in the center of the coil. The sample was consequently evenly heated while also being isolated from any external heat transfer. 2 min, 4 min, 8 min, 12 min, 16min, 20 min, 24 min, and 28 min were compared as durations for the AMF-RF exposure of the samples. Immediately after hysteretic heating, samples were centrifuged (10 min, 1200×g), and three 100  $\mu\text{L}$  aliquots of the supernatant were pipetted per sample into a 96-well plate with 100  $\mu\text{L}$  of PBS added to each well. To evaluate the amount of fluorescein maleimide released by the retro Diels-Alder reaction (Fig. 2), the fluorescence intensity was measured in each well at 494/518 nm (Excitation/Emission) using a Molecular Devices Spectramax M5 Microplate/Cuvette Reader.

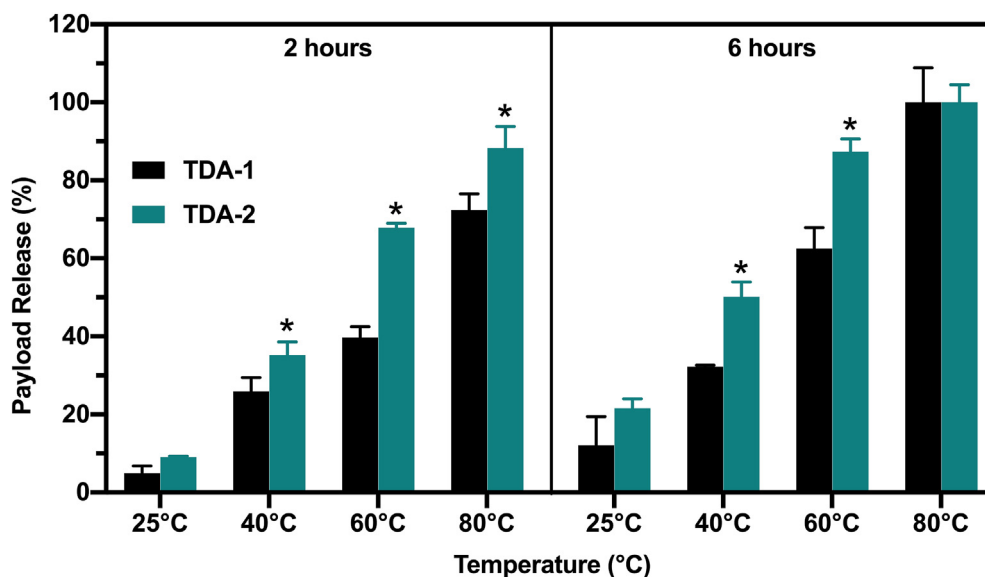


**Fig. 5.** Payload release from  $\text{Fe}_3\text{O}_4$  nanoparticles conjugated with either TDA-1 or TDA-2 after immersion heating ( $n = 3$  per group). \*Significant difference ( $p < 0.05$ ) when compared to TDA-1 for a similar temperature and duration. Additional data for the thermal release water bath immersion study are available in the [Supporting Material Figures S4, S5, S6, and S7](#).

## 2.8. Statistical analysis

Quantitative results were expressed as mean values  $\pm$  standard deviation (SD). Sample size ( $n$ ) is indicated in the figure legends. Statistical analysis was performed via two-way analysis of variance (ANOVA), followed by Tukey's *post hoc* testing. Statistical significance was set at  $p < 0.05$ . The software GraphPad Prism 8 was used for all statistical analyses.

## 3. Results and discussion

### 3.1. Density functional theory computations

DFT calculations were used to determine the forward and reverse energy barriers [42]. Two different thiophene-based dienes were used in this study: 2-Thiophenemethanethiol (T-1) and 4,5-Dimethyl-N-(2-sulfanylethyl)-2-thiophenecarboxamide (T-2). Fluorescein maleimide was the dienophile used for the Diels-Alder reaction (Fig. 1). The enthalpy and Gibbs free energy barriers predicted at different temperatures are reported in Fig. 3 along with the PyMOL [43] rendered images obtained from the B3LYP/6-311G\* computations [31–34]. For each reaction, both the endo and exo products were modeled. It has been shown that electron rich dienes react more favorably with dienophiles than neutral or electron poor dienes [44,45]. T-2 has two methyl substituents, acting as electron donors, while T-1 has an alkyl sulfhydryl group. Therefore, the formation of TDA-2 should have a lower energy barrier compared to that for TDA-1, which agreed with the calculated values for the forward reaction energies of TDA-1 and TDA-2.

In this study, the use of thiophene-based dienes with different substituents dramatically changed the kinetics of the retro Diels-Alder reaction. As reported in the literature [46], methyl substituents on Diels-Alder cycloadducts have been experimentally and computationally shown to increase the exergonicity and reversibility of the Diels-Alder reaction. The location of the methyl substituent on the cycloadduct will also affect the reverse energy barriers. In this study, the electron donating methyl substituents of T-2 on the 4- and especially the 5-position increased the exergonicity and lowered the reverse energy barrier for the TDA-2 retro Diels-Alder reaction. The amide functional group was neutral in character, and therefore had negligible effects on the forward and reverse reaction energies. The synergistic effects of these methyl substituents contributed to the large difference in reverse

reaction energies between the TDA-1 and the TDA-2 cycloadducts. An additional interesting finding from the computational study is the composition dependent differences in the reverse reaction rates of the TDA-1 and TDA-2 endo and exo structures. For TDA-1, the reverse reactions barriers are similar for the endo and exo structures, while in TDA-2 there is an almost 2 kcal/mol difference.

### 3.2. Synthesis and characterization of $\text{Fe}_3\text{O}_4$ nanoparticles

To determine the size and composition of the synthesized nanoparticles, transmission electron microscopy (TEM) imaging and powder X-ray diffraction (XRD) analysis were performed (Fig. 4). The nanoparticles were nearly spherical and clustered together. The majority of the nanoparticles were in the 5–10 nm size range, with some particles over 10 nm in size. These values are in agreement with previously reported coprecipitation synthesis [4,5,37]. For XRD analysis, the software Jade was used and a Rietveld Refinement was performed. Post-analysis, the XRD results showed primarily single phase crystallinity of the  $\text{Fe}_3\text{O}_4$  nanoparticles with over 95% phase purity. The composition of the nanoparticles was determined to be magnetite ( $\text{Fe}_3\text{O}_4$ ) corresponding to the Miller indices reported in Fig. 4. The size distribution of the nanoparticles was determined to be  $10.1 \pm 0.5$  nm in diameter, similar to the size determined by TEM. In studies using the synthetic protocol established by Massart, iron oxide nanoparticles had a size distribution between 5 and 12 nm in diameter [37,47]. In another study, the size distribution was  $10.4 \pm 0.3$  nm indicating that our particles fell in the expected range for this synthesis [4]. The magnetic hysteresis curves for the synthesized iron oxide nanoparticles are also shown in Fig. 4. The magnetic saturation and the anisotropy barrier of the nanoparticles affect the hysteretic losses. For these nanoparticles, the magnetic saturation was 77 emu/g.  $\text{Fe}_3\text{O}_4$  nanoparticles with sizes ranging from 9.1 to 13.1 nm have been reported with magnetic saturations between 70 and 90 emu/g, in good agreement with the results from this study [48].

The alternating magnetic field strength used for this study was measured at 20 kA/m and the radiofrequency used was 624.7 kHz (calculations available in the Supporting Material). The specific loss power (SLP) value was determined to be  $108 \pm 24$  W/g under the specified AMF-RF conditions (calculations available in the Supporting Material). This SLP value aligns with others reported in previous studies [4,5,47,49].

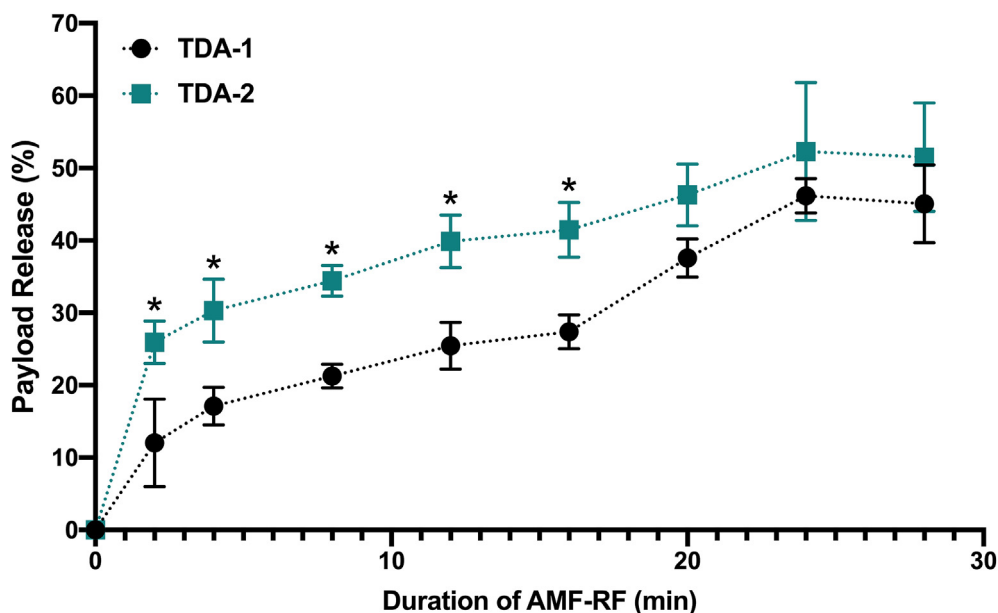


Fig. 6. Payload release from  $\text{Fe}_3\text{O}_4$  nanoparticles conjugated with either TDA-1 or TDA-2 and exposed to AMF-RF hysteretic heating ( $n = 3$  per group). \*Significant difference ( $p < 0.05$ ) when compared to TDA-1 for a similar duration of AMF-RF.

### 3.3. Immersion heating

Water bath immersion studies were performed on  $\text{Fe}_3\text{O}_4$  nanoparticles modified with both TDA-1 and TDA-2 to determine the thermal release profiles (Fig. 5). The temperatures used were 25 °C, 40 °C, 60 °C, or 80 °C and the duration 1 h, 2 h, 4 h, or 6 h. The amount of fluorescein maleimide released by the retro Diels-Alder reaction was measured via fluorescence intensity measurements, and the values were normalized to the nanoparticle samples heated at 80 °C for 6 h. This reference was chosen based on the results of previous release studies from nanoparticles with Diels-Alder cycloadducts where the complete release was being achieved after 2 h at 80 °C [26]. Heat influenced the equilibrium between starting materials and products. The immersion heating results indicated that TDA-2 released fluorescein maleimide more rapidly than TDA-1. This trend occurred for all different temperatures and durations tested. These results correlate with the DFT calculations reported in Fig. 3, where the energy barriers for the reverse reaction of TDA-2 were lower than the energy barriers for TDA-1. 2 and 6 h durations are shown in Fig. 5 but additional data (1 and 4 h duration) are also available in the Supporting Material Figs. S4, S5, S6, and S7.

### 3.4. AMF-RF hysteretic heating

AMF-RF hysteretic heating was performed on the  $\text{Fe}_3\text{O}_4$  nanoparticles modified with TDA-1 and TDA-2 (Fig. 6). The magnetic field strength used for this study was measured ( $n = 3$ ) at 20 kA/m and the radio-frequency used was 624.7 kHz (calculations available in the Supporting Material). The specific loss power (SLP) value was determined ( $n = 3$ ) to be  $108 \pm 24$  W/g under the specified AMF-RF conditions (calculations available in the Supporting Material). This SLP value aligns with others reported in previous studies [4,5,47,49]. All experiments were performed at room temperature (20 °C). The AMF-RF stimulation resulted in a point heating of the nanoparticles rather than a bulk heating of the solution as previously reported [5].

Nanoparticles modified with TDA-2 displayed a higher fluorescein maleimide release rate than the nanoparticles modified with TDA-1. This trend correlated with the release rates observed during the thermal release water bath immersion studies in Fig. 5 and the predicted values of the reverse energy barriers from Fig. 3. For the initial time points, TDA-2 showed a rapid release at 2 and 4 min, followed by a steady increase in

release up to 28 min. TDA-1 had a slower fluorescein maleimide payload release up to 28 min, without the burst release seen in the TDA-2 composition.

The AMF-RF fluorescein maleimide release rates reported in this study are 1.5–2 times the release rates measured in our previous study with similar radiofrequency and magnetic field strength parameters [5]. This could be attributed to the size differences and resulting specific loss power differences of the iron oxide nanoparticles used in each study. In our previous study, the  $\text{Fe}_3\text{O}_4$  nanoparticles had a size distribution of  $7.9 \pm 0.2$  nm in diameter with a SLP value of  $78 \pm 5$  W/g [5]. In this study, the  $\text{Fe}_3\text{O}_4$  nanoparticles had a size distribution of  $10.1 \pm 0.5$  nm in diameter with a SLP value of  $108 \pm 24$  W/g.

## 4. Conclusions

This study describes a tuneable and reproducible controlled release of fluorescein maleimide from the surface of iron oxide nanoparticles via the retro Diels-Alder reaction. Using density functional theory predictions, forward and reverse energy barriers were calculated and revealed a significant difference in reverse energy barriers between the two Diels-Alder linkers. The payload release rates measured for the immersion heating and the AMF-RF hysteretic heating correlated with the modeling results. TDA-2 had a higher payload release rate than TDA-1, with a large amount of payload released after minutes of heat immersion or AMF-RF exposure. Having two distinct Diels-Alder linkers with dramatically different reverse energy barriers and payload release rates broadens the possible delivery applications of thermally reversible linkers. This technology could be expanded into chemical catalysis, supramolecular chemistry, thermoresponsive materials, and temporally controlled drug delivery systems.

### Declaration of competing interest

The authors declare that they have no known competing financial interests or personal relationships that could have appeared to influence the work reported in this paper.

### Acknowledgements

This work was supported by the Office of the Assistant Secretary of

Defense for Health Affairs through the Peer Reviewed Medical Research Program under Award No. W81XWH-18-1-0115. Opinions, interpretations, conclusions and recommendations are those of the authors and are not necessarily endorsed by the Department of Defense. LJ and JCB gratefully acknowledge financial support from National Science Foundation Grant CHE-1856419 and NRT-1449785. Simulations in this work were conducted in part with Advanced Cyber infrastructure computational resources provided by the Institute for Computational and Data Sciences at The Pennsylvania State University (University Park, PA). The authors would like to thank Dr. Tatiana Laremore and the members of the Penn State Proteomics and Mass Spectrometry Facility (University Park, PA) for their assistance with mass spectrometry analyses.

## Appendix A. Supplementary data

Supplementary data to this article can be found online at <https://doi.org/10.1016/j.jciso.2021.100034>.

## References

- [1] C.-S. Wu, T.-H. Kao, H.-Y. Li, Y.-L. Liu, Preparation of polybenzoxazine-functionalized Fe<sub>3</sub>O<sub>4</sub> nanoparticles through in situ Diels-Alder polymerization for high performance magnetic polybenzoxazine/Fe<sub>3</sub>O<sub>4</sub> nanocomposites, *Compos. Sci. Technol.* 72 (13) (2012) 1562–1567.
- [2] S. Schäfer, G. Kickelbick, Diels-Alder reactions on surface-modified magnetite/maghemite nanoparticles: application in self-healing nanocomposites, *ACS Applied Nano Materials* 1 (6) (2018) 2640–2652.
- [3] L. Yi-Huan, Z. Yan-Nian, H.-T. Wang, W. Ming-Feng, K. Wen-Chi, C. Wei-Jen, W. Tun-Fun, R. Syang-Peng, Fabrication of self-healable magnetic nanocomposites via Diels-Alder click chemistry, *Appl. Sci.* 9 (3) (2019).
- [4] T.T.T. N'Guyen, H.T.T. Duong, J. Basuki, V. Montebault, S. Pascual, C. Guibert, J. Fresnais, C. Boyer, M.R. Whittaker, T.P. Davis, L. Fontaine, Functional iron oxide magnetic nanoparticles with hyperthermia-induced drug release ability by using a combination of orthogonal click reactions, *Angew. Chem. Int. Ed.* 52 (52) (2013) 14152–14156.
- [5] J.S. Casey, J.H. Arrizabalaga, M. Abu-Laban, J.C. Becca, B.J. Rose, K.T. Strickland, J.B. Bursavich, J.S. McCann, C.N. Pacheco, L. Jensen, A. Attaluri, D.J. Hayes, Alternating magnetic field mediated release of fluorophores from magnetic nanoparticles by hysteretic heating, *J. Colloid Interface Sci.* 571 (2020) 348–355.
- [6] M. Hammad, V. Nica, R. Hempelmann, On-command controlled drug release by diels-alder reaction using Bi-magnetic core/shell nano-carriers, *Colloids Surf. B Biointerfaces* 150 (2017) 15–22.
- [7] L.-L. Wang, A. Balakrishnan, N.-C. Bigall, D. Candito, J.F. Miethe, K. Seidel, Y. Xie, M. Ott, A. Kirschning, A bio-chemosynthetic approach to superparamagnetic iron oxide-ansamitocin conjugates for use in magnetic drug targeting, *Chem. Eur. J.* 23 (10) (2017) 2265–2270.
- [8] D.V. Baker, K.M. Arafah, A. Asadirad, B. Kaur, R. Raza, N.R. Branda, Photothermal release of an encapsulated therapeutic agent from polymer-wrapped gold nanoparticles, *Nanoscale Advances* (2021).
- [9] A.B.S. Bakhtiari, D. Hsiao, G. Jin, B.D. Gates, N.R. Branda, An efficient method based on the photothermal effect for the release of molecules from metal nanoparticle surfaces, *Angew. Chem. Int. Ed.* 48 (23) (2009) 4166–4169.
- [10] R.R. Kumal, M. Abu-Laban, P. Hamal, B. Kruger, H.T. Smith, D.J. Hayes, L.H. Haber, Near-infrared photothermal release of siRNA from the surface of colloidal gold-silver-gold core-shell nanoparticles studied with second-harmonic generation, *J. Phys. Chem. C* 122 (34) (2018) 19699–19704.
- [11] R.R. Kumal, M. Abu-Laban, C.R. Landry, B. Kruger, Z. Zhang, D.J. Hayes, L.H. Haber, Plasmon-enhanced photocleaving dynamics in colloidal MicroRNA-functionalized silver nanoparticles monitored with second harmonic generation, *Langmuir* 32 (40) (2016) 10394–10401.
- [12] R.R. Kumal, C.R. Landry, M. Abu-Laban, D.J. Hayes, L.H. Haber, Monitoring the photocleaving dynamics of colloidal MicroRNA-functionalized gold nanoparticles using second harmonic generation, *Langmuir* 31 (36) (2015) 9983–9990.
- [13] N. Basavegowda, K. Mishra, Y.R. Lee, Y.-G. Joh, Magnetically separable iron oxide nanoparticles: an efficient and reusable catalyst for imino diels-alder reaction, *Bull. Kor. Chem. Soc.* 37 (2) (2016) 142–147.
- [14] X. Li, S. Zhang, B. Yang, C. Lv, X. Jia, Z. Hu, Magnetic Fe<sub>3</sub>O<sub>4</sub> nanoparticles supporting Macmillan with controlled shell structure as an efficient and reusable catalyst for asymmetric reaction, *RSC Adv.* 6 (89) (2016) 86531–86539.
- [15] M.B. Schütz, K. Lê, S. Ilyas, S. Mathur, Reversible covalent assembly of nanoparticles through on-surface diels-alder reaction, *Langmuir* 36 (6) (2020) 1552–1558.
- [16] A. Chiu-Lam, C. Rinaldi, Nanoscale thermal phenomena in the vicinity of magnetic nanoparticles in alternating magnetic fields, *Adv. Funct. Mater.* 26 (22) (2016) 3933–3941.
- [17] T. Blin, A. Niederberger, L. Benyahia, J. Fresnais, V. Montebault, L. Fontaine, Thermoresponsive hybrid double-crosslinked networks using magnetic iron oxide nanoparticles as crossing points, *Polym. Chem.* 9 (37) (2018) 4642–4650.
- [18] Y. Oz, A. Sanyal, The taming of the maleimide: fabrication of maleimide-containing 'clickable' polymeric materials, *Chem. Rec.* 18 (6) (2018) 570–586.
- [19] C. Meng, W. Zhikun, L. Qiang, L. Chunling, S. Shuangqing, H. Songqing, Preparation of amino-functionalized Fe<sub>3</sub>O<sub>4</sub>@mSiO<sub>2</sub> core-shell magnetic nanoparticles and their application for aqueous Fe<sup>3+</sup> removal, *J. Hazard Mater.* 341 (2018) 198–206.
- [20] S. Deka, V. Saxena, A. Hasan, P. Chandra, L.M. Pandey, Synthesis, characterization and in vitro analysis of  $\alpha$ -Fe<sub>2</sub>O<sub>3</sub>-GdFeO<sub>3</sub> biphasic materials as therapeutic agent for magnetic hyperthermia applications, *Mater. Sci. Eng. C* 92 (2018) 932–941.
- [21] A. Maleki, R. Taheri-Ledari, M. Soroushnejad, Surface functionalization of magnetic nanoparticles via palladium-catalyzed Diels-Alder approach, *Chemistry* 3 (46) (2018) 13057–13062.
- [22] A. Maleki, M. Aghaei, H.R. Hafizi-Atabak, M. Ferdowsi, Ultrasonic treatment of CoFe<sub>2</sub>O<sub>4</sub>@B<sub>2</sub>O<sub>3</sub>-SiO<sub>2</sub> as a new hybrid magnetic composite nanostructure and catalytic application in the synthesis of dihydroquinazolinones, *Ultrason. Sonochem.* 37 (2017) 260–266.
- [23] L. Xiao, M. Mertens, L. Wortmann, S. Kremer, M. Valldor, T. Lammers, F. Kiessling, S. Mathur, Enhanced in vitro and in vivo cellular imaging with green tea coated water-soluble iron oxide nanocrystals, *ACS Appl. Mater. Interfaces* 7 (12) (2015) 6530–6540.
- [24] A. Hervault, N.T.K. Thanh, Magnetic nanoparticle-based therapeutic agents for thermo-chemotherapy treatment of cancer, *Nanoscale* 6 (20) (2014) 11553–11573.
- [25] K.E. Horner, P.B. Karadakov, Chemical bonding and aromaticity in furan, pyrrole, and thiophene: a magnetic shielding study, *J. Org. Chem.* 78 (16) (2013) 8037–8043.
- [26] M. Abu-Laban, R.R. Kumal, J. Casey, J. Becca, D. Lamaster, C.N. Pacheco, D.G. Sykes, L. Jensen, L.H. Haber, D.J. Hayes, Comparison of thermally actuated retro-diels-alder release groups for nanoparticle based nucleic acid delivery, *J. Colloid Interface Sci.* 526 (2018) 312–321.
- [27] M. Abu-Laban, P. Hamal, J.H. Arrizabalaga, A. Forghani, A.S. Dikkumbura, R.R. Kumal, L.H. Haber, D.J. Hayes, Combinatorial delivery of miRNA-nanoparticle conjugates in human adipose stem cells for amplified osteogenesis, *Small* 15 (50) (2019) 1902864.
- [28] Y. Liu, J.T. Bailey, M. Abu-Laban, S. Li, C. Chen, A.B. Glick, D.J. Hayes, Photocontrolled miR-148b nanoparticles cause apoptosis, inflammation and regression of Ras induced epidermal squamous cell carcinomas in mice, *Biomaterials* 256 (2020) 120212.
- [29] S. He, G. Kickelbick, Reversible diels-alder reactions with a fluorescent dye on the surface of magnetite nanoparticles, *Molecules* 26 (4) (2021) 877.
- [30] E. Aprà, E.J. Bylaska, W.A. De Jong, N. Govind, K. Kowalski, T.P. Straatsma, M. Valiev, H.J.J. Van Dam, Y. Alexeev, J. Anchell, V. Anisimov, F.W. Aquino, R. Atta-Fynn, J. Autschbach, N.P. Bauman, J.C. Becca, D.E. Bernholdt, K. Bhaskaran-Nair, S. Bogatko, P. Borowski, J. Boschen, J. Brabec, A. Bruner, E. Cui, Y. Chen, G.N. Chuev, C.J. Cramer, J. Daily, M.J.O. Deegan, T.H. Dunning, M. Dupuis, K.G. Dyall, G.I. Fann, S.A. Fischer, A. Fonari, H. Früchtl, L. Gagliardi, J. Garza, N. Gawande, S. Ghosh, K. Glaesemann, A.W. Götz, J. Hammond, V. Helms, E.D. Hermes, K. Hirao, S. Hirata, M. Jacquelin, L. Jensen, B.G. Johnson, H. Jönsson, R.A. Kendall, M. Klemm, R. Kobayashi, V. Konkov, S. Krishnamoorthy, M. Krishnan, Z. Lin, R.D. Lins, R.J. Littlefield, A.J. Logsdail, K. Lopata, W. Ma, A.V. Marenich, J. Martin Del Campo, D. Mejia-Rodriguez, J.E. Moore, J.M. Mullin, T. Nakajima, D.R. Nascimento, J.A. Nichols, P.J. Nichols, J. Nieplocha, A. Otero-De-La-Rozza, B. Palmer, A. Panyala, T. Pirojnsirakul, B. Peng, R. Peverati, J. Pittner, L. Pollack, R.M. Richard, P. Sadayappan, G.C. Schatz, W.A. Shelton, D.W. Silverstein, D.M.A. Smith, T.A. Soares, D. Song, M. Swart, H.L. Taylor, G.S. Thomas, V. Tipparaju, D.G. Truhlar, K. Tsemekhan, T. Van Voorhis, Á. Vázquez-Mayagoitia, P. Verma, O. Villa, A. Vishnu, K.D. Vogiatzis, D. Wang, J.H. Weare, M.J. Williamson, T.L. Windus, K. Wolinski, A.T. Wong, C. Wu, C. Yang, Q. Yu, M. Zacharias, Z. Zhang, Y. Zhao, R.J. Harrison, *NWChem: past, present, and future*, *J. Chem. Phys.* 152 (18) (2020) 184102.
- [31] A.D. Becke, Density-functional thermochemistry. III. The role of exact exchange, *J. Chem. Phys.* 98 (7) (1993) 5648–5652.
- [32] S.H. Vosko, L. Wilk, M. Nusair, Accurate spin-dependent electron liquid correlation energies for local spin density calculations: a critical analysis, *Can. J. Phys.* 58 (8) (1980) 1200–1211.
- [33] C. Lee, W. Yang, R.G. Parr, Development of the Colle-Salvetti correlation-energy formula into a functional of the electron density, *Phys. Rev. B* 37 (2) (1988) 785–789.
- [34] P.J. Stephens, F.J. Devlin, C.F. Chabalowski, M.J. Frisch, Ab initio calculation of vibrational absorption and circular dichroism spectra using density functional force fields, *J. Phys. Chem.* 98 (45) (1994) 11623–11627.
- [35] A. Abiko, J.C. Roberts, T. Takemasa, S. Masamune, KMnO<sub>4</sub> revisited: oxidation of aldehydes to carboxylic acids in the *n*-butyl alcohol - aqueous NaH<sub>2</sub>PO<sub>4</sub> system, *Tetrahedron Lett.* 27 (38) (1986) 4537–4540.
- [36] C. Xu, J. Xie, D. Ho, C. Wang, N. Kohler, E.G. Walsh, J.R. Morgan, Y.E. Chin, S. Sun, Au-Fe<sub>3</sub>O<sub>4</sub> dumbbell nanoparticles as dual-functional probes, *Angew. Chem. Int. Ed.* 47 (1) (2008) 173–176.
- [37] R. Massart, Preparation of aqueous magnetic liquids in alkaline and acidic media, *IEEE Trans. Magn.* 17 (2) (1981) 1247–1248.
- [38] H. Cao, J. He, L. Deng, X. Gao, Fabrication of cyclodextrin-functionalized superparamagnetic Fe<sub>3</sub>O<sub>4</sub>/amino-silane core-shell nanoparticles via layer-by-layer method, *Appl. Surf. Sci.* 255 (18) (2009) 7974–7980.
- [39] C. Xu, K. Xu, H. Gu, R. Zheng, H. Liu, X. Zhang, Z. Guo, B. Xu, Dopamine as a Robust anchor to immobilize functional molecules on the iron oxide shell of magnetic nanoparticles, *J. Am. Chem. Soc.* 126 (32) (2004) 9938–9939.
- [40] R.E. Rosensweig, Heating magnetic fluid with alternating magnetic field, *J. Magn. Magn. Mater.* 252 (1–3) (2002) 370–374.
- [41] F. Soetaert, S.K. Kandal, A. Bakuzis, R. Ivkov, Experimental estimation and analysis of variance of the measured loss power of magnetic nanoparticles, *Sci. Rep.* 7 (1) (2017).



- [42] V. Guner, K.S. Khuong, A.G. Leach, P.S. Lee, M.D. Bartberger, K.N. Houk, A standard set of pericyclic reactions of hydrocarbons for the benchmarking of computational methods: the performance of ab initio, density functional, CASSCF, CASPT2, and CBS-QB3 methods for the prediction of activation barriers, reaction energetics, and J. Phys. Chem. 107 (51) (2003) 11445–11459.
- [43] W.L. Delano, PyMOL: an open-source molecular graphics tool, CCP4 Newsletter on protein crystallography 40 (1) (2002) 82–92.
- [44] J. Sauer, R. Sustmann, Mechanistic aspects of diels-alder reactions: a critical survey, Angew. Chem. Int. Ed. Engl. 19 (10) (1980) 779–807.
- [45] A. Padwa, K.R. Crawford, C.S. Straub, S.N. Pieniazek, K.N. Houk, Halo substituent effects on intramolecular cycloadditions involving furanyl amides, J. Org. Chem. 71 (15) (2006) 5432–5439.
- [46] R.C. Boutele, B.H. Northrop, Substituent effects on the reversibility of furan–maleimide cycloadditions, J. Org. Chem. 76 (19) (2011) 7994–8002.
- [47] J.-P. Fortin, C. Wilhelm, J. Servais, C. Ménager, J.-C. Bacri, F. Gazeau, Size-sorted anionic iron oxide nanomagnets as colloidal mediators for magnetic hyperthermia, J. Am. Chem. Soc. 129 (9) (2007) 2628–2635.
- [48] R. Chen, M.G. Christiansen, P. Anikeeva, Maximizing hysteretic losses in magnetic ferrite Nanoparticles via Model-driven synthesis and materials optimization, ACS Nano 7 (10) (2013) 8990–9000.
- [49] J.-H. Lee, J.-T. Jang, J.-S. Choi, S.H. Moon, S.-H. Noh, J.-W. Kim, J.-G. Kim, I.-S. Kim, K.I. Park, J. Cheon, Exchange-coupled magnetic nanoparticles for efficient heat induction, Nat. Nanotechnol. 6 (7) (2011) 418–422.